.

Probing electron density across Ar$^+$ irradiation-induced self-organized TiO$_{2-x}$ nanochannels for memory application

A. Barman, C. P. Saini, P. K. Sarkar, A. Roy, B. Satpati, D. Kanjilal, S. K. Ghosh, S. Dhar, and A. Kanjilal'

Probing electron density across Ar$^+$ irradiation-induced self-organized TiO$_{2-x}$ nanochannels for memory application

A. Barman,[1] C. P. Saini,[1] P. K. Sarkar,[2] A. Roy,[2] B. Satpati,[3] D. Kanjilal,[4] S. K. Ghosh,[1] S. Dhar,[1] and A. Kanjilal[1,a)]

[1]Department of Physics, School of Natural Sciences, Shiv Nadar University, NH-91, Tehsil Dadri, Gautam Buddha Nagar, Uttar Pradesh 201314, India
[2]Department of Physics, National Institute of Technology, Silchar, Assam 788010, India
[3]Surface Physics and Material Science Division, Saha Institute of Nuclear Physics, 1/AF Bidhannagar, Kolkata 700064, India
[4]Inter University Accelerator Centre, Aruna Asaf Ali Marg, New Delhi 110067, India

The variation of electron density in TiO$_{2-x}$ nanochannels, exhibiting resistive switching phenomenon, produced by Ar$^+$ ion-irradiation at the threshold fluence of 5×10^{16} ions/cm^2 is demonstrated by X-ray reflectivity (XRR). The transmission electron microscopy reveals the formation of nanochannels, while the energy dispersive X-ray spectroscopy confirms Ti enrichment near the surface due to ion-irradiation, in consistent with the increase in electron density by XRR measurements. Such a variation in Ti concentration indicates the evolution of oxygen vacancies (OVs) along the TiO$_{2-x}$ nanochannels, and thus paves the way to explain the operation and performance of the Pt/TiO$_{2-x}$/Pt-based memory devices via OV migration. *Published by AIP Publishing.*
[http://dx.doi.org/10.1063/1.4954166]

Transition metal oxides (TMOs) have laid an important platform in the field of oxide electronics for their easy integration and compatibility with the present Si technology.[1–3] The role of TMOs, such as TiO$_2$, Ta$_2$O$_5$, HfO$_2$, WO$_2$, etc., has further been boosted for memory applications, especially in resistive switching (RS) devices.[3–6] Apart from the commonly used binary oxides, complex oxides, such as BaTiO$_3$, SrTiO$_3$, carbon-based oxides, and organic materials, have also attracted much attention for memory research.[7–10] Among the many potential binary oxides, TiO$_2$ has extensively been studied for RS application where the underlying mechanism has mostly been discussed in the light of oxygen vacancy (OV) migration toward positive electrode followed by retraction due to altering the potential to negative.[11,12] However, controlled introduction of OVs requires further attention for enhancing device performance, especially in miniaturized structures. Several attempts have already been made for intentional creation of OVs in the near surface region of TiO$_2$ thin films either by varying oxygen partial pressure during deposition or by irradiating with energetic ions.[11,13]

It has been observed that the formation and distribution of OVs in anatase (A-TiO$_2$) and rutile (R-TiO$_2$) are, however, significantly different due to the diffusion of Ti interstitials toward the surface in the latter case, than that of energetically favorable OVs in the bulk of A-TiO$_2$ layers.[14–16] Therefore, ion beam irradiation technique offers a better choice to control the introduction of OVs over depth in TiO$_2$ films with appropriate choice of ion species, energy, and fluence (i.e., ions/cm^2). In fact, we have recently shown the formation of TiO/Ti$_2$O$_3$ mix-phases and so the oxygen deficient region near the surface by exposing the polycrystalline TiO$_2$ layers to 50 keV Ar$^+$-ions at an ion fluence of 5×10^{16} ions/cm^2.[11] The local

RS behavior has been demonstrated by *ex-situ* conductive atomic force microscopy (c-AFM) and explained in terms of field-driven migration of OVs.[11] This could be due to the higher OV concentration induced development of local conducting filament along the grain boundaries with respect to grains as was predicted earlier by *in-situ* c-AFM measurements.[17,18] Moreover, the evolution of voids and the existence of TiO$_{2-x}$ were confirmed by cross-sectional transmission electron microscopy (XTEM), though depth-dependent compositional variation was not prominent. It is therefore essential to use a suitable technique to do so. In this respect, X-ray reflectivity (XRR) measurement is known to be a non-destructive process and also a powerful tool for understanding the overall structures of stratified samples and the interfacial roughness by investigating the electron density (ρ) as a function of depth. Since any change in chemical structure of TiO$_2$ can lead to the formation of OVs, XRR would be preferable for determining ion-beam induced modification of ρ with depth, and the possible change in sample compositions.

In this letter, the formation of nanochannels through evolution of voids in polycrystalline TiO$_{2-x}$ layers by bombarding with 50 keV Ar$^+$-ions at a fluence of 5×10^{16} ions/cm^2 has been explored by XTEM, while depth-dependent change in chemical properties was examined by XRR through determination of ρ using Parratt's algorithm.[19] Beside these studies, detailed electrical properties have been reported toward real time application as resistive random access memory (RRAM) devices.

About 75 nm thick TiO$_{2-x}$ thin films have been grown on Pt/Ti/SiO$_2$/Si substrates at room temperature (RT) using radio frequency magnetron sputtering technique. Prototype devices have been fabricated by depositing Pt top electrodes (TEs) of diameter 500 μm (area: $\sim 2 \times 10^5$ μm^2) on TiO$_{2-x}$ film using shadow masking in an electron beam deposition system. Before the formation of TEs, the as-grown TiO$_{2-x}$

a)Electronic mail: aloke.kanjilal@snu.edu.in

films were irradiated at RT with 50 keV Ar$^+$-ions at normal incidence. The detailed deposition process and irradiation technique are reported in Ref. 11. The pristine sample is referred as S0, while the samples irradiated with fluences of 5×10^{14}, 1×10^{15}, 1×10^{16}, and 5×10^{16} ions/cm^2 are represented by S1, S2, S3, and S4, respectively. Ion beam induced modification of microstructure has initially been investigated by TEM (using 300 keV FEI Tecnai G^2 S-Twin system) in cross-sectional geometry. Moreover, XRR has been performed in a systematic way using a Bruker-D8 Discover X-ray diffractometer with a source of 8.5 keV energy where the reflectivity data have been collected by maintaining equal incident angle (α_i) and exit angle (α_f), and by keeping the horizontal scattering angle to zero.[20] The scattered X-ray beam has been detected with a 1D X-ray detector (LYNXEYE XE) with varying α_i. At this specular condition ($\alpha_i = \alpha_f$), the perpendicular component of momentum transfer vector (q_z) provides structural information of the sample in the vertical direction. The data were fitted by Parratt's algorithm to extract ρ as a function of depth (z).[21] To investigate the device performance and reproducibility, current–voltage (I-V) characteristics have been monitored by semiconductor parameter analyzer (Keithley 4200-SCS) in seven different devices, while the top and bottom electrodes have been biased and grounded, respectively.

Figure 1(a) shows the XTEM image exhibiting the presence of TiO$_{2-x}$ nanochannels in between the voids (in white) at a fluence of 5×10^{16} ions/cm^2. Small voids are also visible in the matrix, while they are mainly concentrated deep inside the TiO$_{2-x}$ layers. The magnified view of those is depicted in Fig. 1(b), displaying one of such nanochannels. Previously, the energy-filtered TEM study revealed the existence of oxygen deficient TiO$_2$ zone in the near surface region, whereas X-ray photoelectron spectroscopy (XPS) investigation showed the formation of Ti^{2+}/Ti^{3+} oxidation state of Ti in this region.[11] The change in elemental concentration across the thickness of Ar$^+$-ion irradiated TiO$_{2-x}$ layers has been examined by energy

dispersive X-ray spectroscopy (EDX) when acquiring high-angle annular dark-field (HAADF) images as the one shown in Fig. 1(c). The typical elemental profiles of Si-*K*, O-*K*, Pt-*M*, Ti-*K*, and Ar-*K* edges from the EDX trace [shown by downward arrow in Fig. 1(c)] are exhibited in Fig. 1(d). As can be seen from Fig. 1(d), the Ti concentration increases near the surface as compared with that in the inner layers of TiO$_{2-x}$ films. One should note here that as the EDX spectra have been acquired starting from the glue to underneath Pt layer [see Fig. 1(c)], the actual sample surface can be found 50 nm down the line as seen in Fig. 1(d). A sudden drop of Ti concentration up to ~100 nm depth can be assigned to the void region, while it increases again up to ~150 nm till reaching the Pt surface, followed by a sharp rise at ~310 nm for buffer Ti layer [see Fig. 1(a)]. The observed increase in Ti signal near the surface of the TiO$_{2-x}$ layers is most likely associated with the preferential sputtering of O due to low surface binding energy with respect to Ti atoms. Since cross-sectional line scan provides atomic distribution within a few nanometer regions, XRR has been employed to determine the spatial atomic concentrations as a function of depth from the sample surface.

A typical set of reflectivity data of Ar$^+$-ion bombarded TiO$_{2-x}$/Pt/Ti/SiO$_2$/Si structures with varying ion-fluence is exhibited in Fig. 2(a). Using Parratt's algorithm, a MATLAB code has been developed for fitting the experimental data (shown by solid lines in Fig. 2(a)) by varying three parameters, i.e., electron density (ρ), layer thickness (t), and the interface roughness (σ) within physically acceptable values.[22] The simulated results are summarized in Table I. In the case of un-irradiated samples (S0), two sub-layers have been considered for the best fit: the top TiO$_{2-x}$ layer with a thickness of ~75 nm and fixed electron density of 1.38 e$^-$/Å^3, while the bottom 200 nm thick Pt layer considered as of infinite thickness. The other layers lying below the Pt have not been considered in this calculation as the maximum X-ray penetration depth is estimated to be confined within the Pt layer for highest q_z value. However, the ion-irradiated samples could not be
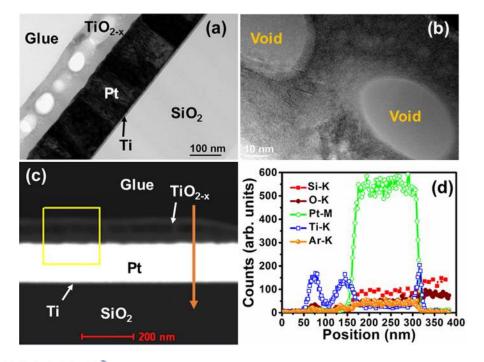

FIG. 1. (a) Bright field XTEM image of sample irradiated with 5×10^{16} ions/cm^2 (S4); (b) HRTEM image of S4 taken at one of the nanochannels surrounded by voids; (c) HAADF image for S4, and the downward arrow represents the direction along which the EDX trace has been taken; (d) the typical elemental profiles of Si-*K*, O-*K*, Pt-*M*, Ti-*K*, and Ar-*K* edges along the EDX trace as a function of depth from the sample surface at ~50 nm.
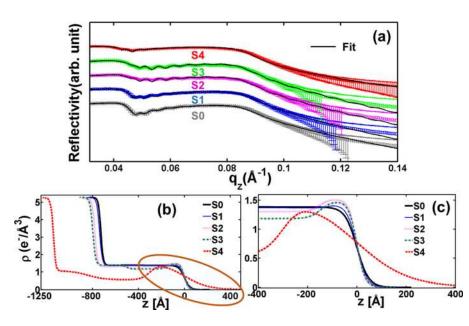
FIG. 2. (a) XRR data from samples before (S0) and after irradiation with fluences of 5×10^{14} (S1), 1×10^{15} (S2), 1×10^{16} (S3), and 5×10^{16} (S4) ions/cm^2 as function of momentum vector (q_z) with corresponding fitted curves in solid lines; (b) electron density (ρ) before and after Ar$^+$-ion irradiation as a function of sample depth (z), and (c) the magnified view of the circled (saffron colored) area in (b) shows ρ near the surface. The ρ of S4 is smeared off due to huge surface roughness of ~ 18 nm.

fitted by considering a single layer of TiO$_{2-x}$ with uniform ρ on Pt as the one used for S0. Instead, multiple sub-layers with varying ρ have been considered to satisfy the critical angles of the recorded reflectivity profiles. The change in ρ arises from the ion beam induced redistributions and sputtering of the constituent atoms, especially O for its lower surface binding energy with respect to Ti atoms, leading to Ti rich surface layers.[11,23] For instance, two TiO$_{2-x}$ layers with different ρ values have been considered for S1 and S2 while for both S3 and S4 three sub-layers have been chosen. The simulated data in Table I and obtained electron density profiles depicted in Fig. 2(b) clearly show that the ρ of the top TiO$_{2-x}$ surface layer slowly increases with increasing ion fluence. In fact, the ion beam induced variations of ρ in the near

surface region are clearly visible from the magnified view of the circled area of Fig. 2(b) [see Fig. 2(c)] where the air–surface interface is indicated by 0 Å in abscissa. It should be noted that the broad hump in S4 is due to the existence of higher surface roughness; this smears the electron density profile that finally extends beyond the surface of TiO$_{2-x}$ layer. A significant drop of ρ just below the surface of S3 [Fig. 2(c)] can be attributed to the formation of voids. The reduction of ρ is more prominent in S4 and can be attributed to the existence of larger voids as observed in TEM studies [see Fig. 1(a)]. It is therefore clear that the swelling of TiO$_{2-x}$ layers in the ion beam irradiated samples is due to the evolution of voids with increasing fluence.

The extracted value of ρ for S0 (see Table I) is similar to the theoretical value of 1.3 e$^-$/Å^3 for oxygen deficient TiO$_{2-x}$ (or equivalently Ti$_2$O$_3$) layers[24] containing dominant anatase phase ($2\theta \sim 25.4°$) along with some amount of rutile and other phases as perceived from XRD analyses.[11] It may be noted here that the theoretical ρ values of anatase and rutile TiO$_2$ are 1.121 and 1.225 e$^-$/Å^3, respectively.[24,25] As discussed above, the value of ρ after ion-irradiation has been found to be increased significantly with increasing ion fluence. For the highest fluence sample (S4), the surface layer ρ is found to be of 1.55 e$^-$/Å^3 which could be due to the presence of mixed phases of TiO ($\rho \sim 1.65$ e$^-$/Å^3) and Ti$_2$O$_3$ ($\rho \sim 1.3$ e$^-$/Å^3) as previously observed in XPS analyses.[11] This variation in ρ with increasing ion fluence should have a direct impact on RS property which will be discussed in the following by analyzing the Pt/TiO$_{2-x}$/Pt device structure after irradiating with the highest fluence.

Figure 3 demonstrates the electrical performances, such as dc loop, retention, and endurance, along with possible charge conduction mechanisms. Typical bipolar $I–V$ characteristics can be revealed in Fig. 3(a) for S4, showing a forming-free clock-wise RS behavior under a dc sweeping mode from -1 to $+1$ V at RT. It is interesting to note that this device shows a self-compliance bipolar RS behavior within ± 1 V and thus could be useful for low power non-volatile memory (NVM) application. The current flows through this device increases significantly at -0.5 V (V_{set}), consequently
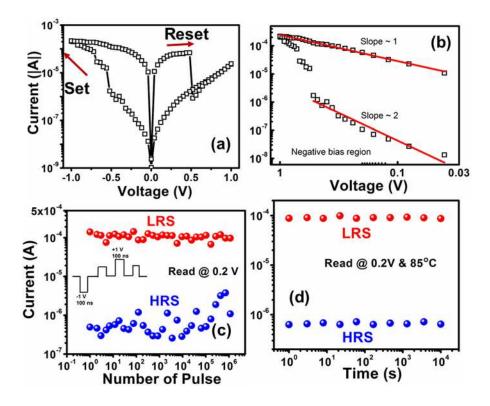
TABLE I. Layer/sub-layer thickness with corresponding electron density (ρ) and interfacial roughness (σ) extracted from XRR fitting.

Samples	Layer from top surface	Layer thickness (Å)	Electron density (e$^-$/Å^3)	Interfacial roughness (Å)
S0	TiO$_{2-x}$	728	1.38	43.46
	Pt	∞	5.28	18.93
S1	TiO$_{2-x}$	117.6	1.43	36.71
	TiO$_{2-x}$	629	1.36	27.54
	Pt	∞	5.28	21.49
S2	TiO$_{2-x}$	150	1.55	30.00
	TiO$_{2-x}$	630	1.28	34.99
	Pt	∞	5.22	21.19
S3	TiO$_{2-x}$	147	1.49	30.59
	TiO$_{2-x}$ (Voids region)	356	1.18	40.80
	TiO$_{2-x}$	294	1.39	29.19
	Pt	∞	5.28	22.27
S4	TiO$_{2-x}$	300	1.55	189.9
	TiO$_{2-x}$ (Voids region)	540	0.56	69.99
	TiO$_{2-x}$	300	1.08	13.00
	Pt mixed with TiO$_{2-x}$	349	5.07	17.50
	Pt	∞	5.28	10.49

FIG. 3. (a) Represents the dc loop of the Pt/TiO$_{2-x}$/Pt devices after Ar$^+$-ion irradiation at a fluence of 5×10^{16} ions/cm^2 while (b) shows the Ohmic and SCLC conduction mechanisms at LRS and HRS in SET, respectively; (c) represents the endurance property of S4 with a read voltage at 0.2 V, while (d) displays the corresponding retention behavior at 85 °C showing considerable potential for NVM application.

switching the device to ON state or low resistance state (LRS). After removing the applied bias, the device continues to stay in LRS. During RESET operation, the device has been reprogrammed to the high resistance state (HRS) at +0.49 V (V_{reset}). The consistency in dc cycle mode has been reported in our previous work.[11]

To know more about the charge transport mechanism of the device, the *I-V* characteristic in SET is re-plotted in log–log scale, where the experimental data points have been fitted with appropriate conduction models,[26,27] as shown in Fig. 3(b). It is evident from the fitting that the device follows a space charge limited conduction (SCLC) in HRS with $dV/dI = 2$, confirming the semiconducting nature of the device.[26] On the other hand, the conduction mechanism is Ohmic in nature with $dV/dI = 1.01$ at LRS.[27] It is attributed to the formation of conducting filamentary path by the OVs in the TiO$_{2-x}$ nanochannels during SET process, and in turn allows the charge carriers to flow linearly giving rise to an Ohmic conduction, as shown by the upper fitted line in Fig. 3(b). While increasing the positive bias voltage, the device attains to the RESET due to rupture of the aligned OVs across the electrodes through nanochannels. This can be connected with the rising temperature due to Joule heating resulting from the enormous linear current flow along the Ohmic conduction path.[28] Furthermore, the endurance and retention properties of S4 device are illustrated in Figs. 3(c) and 3(d). Fig. 3(c) shows the endurance characteristics of S4 up to 10^6 cycles indicating considerable device stability. During the endurance test, S4 device has maintained the HRS/LRS ratio of $\sim 10^3$ without any substantial electrical degradation. Figure 3(d) shows the retention property of S4 device with a rewriting capability over a 10^4 s test period at 85 °C. Both the memory states are distinguishable under the constant voltage stress at 0.2 V and remain stable without any significant degradation over 10^4 s. This indicates the

potential of this device for NVM application as compared with the data reported recently.[29,30]

In conclusion, using XRR analyses we have determined the electron densities (ρ) of the oxygen deficient TiO$_{2-x}$/Pt/Ti/SiO$_2$/Si samples, exhibiting RS behavior, formed after 50 keV Ar$^+$ ion irradiation in the fluence range of $(0.05–5) \times 10^{16}$ ions/cm^2. From the XRR analyses, ρ values determined near the surfaces of ion irradiated samples with increasing fluences in the range of 1.43–1.55 e$^-$/Å^3 have been attributed to the presence of oxygen vacancies in the TiO$_{2-x}$ layers. This is found to be consistent with the EDX data. The fabricated device using the highest fluence sample has shown not only the self-compliance behavior, but also forming free clock-wise RS behavior at lower voltage. The electrical characteristics suggest an Ohmic conduction mechanism in LRS, while SCLC mechanism in HRS. Moreover, the observed endurance and retention behaviors of the device read at 0.2 V opens up the possibility for low power non-volatile memory application.

[1]R. A. McKee, F. J. Walker, and M. F. Chisholm, Phys. Rev. Lett. **81**, 3014 (1998).
[2]T. E. Kazior, Philos. Trans. R. Soc., A **372**, 20130105 (2014).
[3]H.-S. P. Wong, H.-Y. Lee, S. Yu, Y.-S. Chen, Y. Wu, P.-S. Chen, B. Lee, F. T. Chen, and M.-J. Tsai, Proc. IEEE **100**, 1951 (2012).
[4]M. Trapatseli, D. Carta, A. Regoutz, A. Khiat, A. Serb, I. Gupta, and T. Prodromakis, J. Phys. Chem. C **119**, 11958 (2015).
[5]W. D. Song, J. F. Ying, W. He, V. Y.-Q. Zhuo, R. Ji, H. Q. Xie, S. K. Ng, S. L. G. Ng, and Y. Jiang, Appl. Phys. Lett. **106**, 031602 (2015).

[6]V. Iglesias, M. Lanza, K. Zhang, A. Bayerl, M. Porti, M. Nafría, X. Aymerich, G. Benstetter, Z. Y. Shen, and G. Bersuker, Appl. Phys. Lett. **99**, 103510 (2011).

[7]Y. Heo, D. Kan, Y. Shimakawa, and J. Seidel, Phys. Chem. Chem. Phys. **18**, 197 (2016).

[8]P. Predeep, D. Devasia, J. Aneesh, and N. M. Faseena, Microelectron. Eng. **107**, 54 (2013).

[9]E. Mikheev, J. Hwang, A. P. Kajdos, A. J. Hauser, and S. Stemmer, Sci. Rep. **5**, 11079 (2015).

[10]P. Hazra, A. N. Resmi, and K. B. Jinesh, Appl. Phys. Lett. **108**, 153503 (2016).

[11]A. Barman, C. P. Saini, P. Sarkar, B. Satpati, S. R. Bhattacharyya, D. Kabiraj, D. Kanjilal, S. Dhar, and A. Kanjilal, J. Appl. Phys. **118**, 224903 (2015).

[12]N. Ghenzi, M. J. Rozenberg, R. Llopis, P. Levy, L. E. Hueso, and P. Stoliar, Appl. Phys. Lett. **106**, 123509 (2015).

[13]H. Wylezich, H. Mähne, J. Rensberg, C. Ronning, P. Zahn, S. Slesazeck, and T. Mikolajick, ACS Appl. Mater. Interfaces **6**, 17474 (2014).

[14]C. P. Saini, A. Barman, B. Satpati, S. R. Bhattacharyya, D. Kanjilal, and A. Kanjilal, Appl. Phys. Lett. **108**, 011907 (2016).

[15]S. Wendt, P. T. Sprunger, E. Lira, G. K. H. Madsen, Z. Li, J. Ø. Hansen, J. Matthiesen, A. Blekinge-Rasmussen, E. Lægsgaard, B. Hammer, and F. Besenbacher, Science **320**, 1755 (2008).

[16]H. Cheng and A. Selloni, Phys. Rev. B **79**, 092101 (2009).

[17]M. Lanza, K. Zhang, M. Porti, M. Nafría, Z. Y. Shen, L. F. Liu, J. F. Kang, D. Gilmer, and G. Bersuker, Appl. Phys. Lett. **100**, 123508 (2012); M. Lanza, G. Bersuker, M. Porti, E. Miranda, M. Nafría, and X. Aymerich, *ibid.* **101**, 193502 (2012).

[18]M. Lanza, Materials **7**, 2155 (2014).

[19]J. Als-Nielsen and D. McMorrow, *Elements of Modern X-Ray Physics* (John Wiley & Sons, 2011).

[20]S. K. Ghosh, S. Castorph, O. Konovalov, R. Jahn, M. Holt, and T. Salditt, New J. Phys. **12**, 105004 (2010).

[21]L. G. Parratt, Phys. Rev. **95**, 359 (1954).

[22]S. W. Chen, X. Lu, E. Blackburn, V. Lauter, H. Ambaye, K. T. Chan, E. E. Fullerton, A. E. Berkowitz, and S. K. Sinha, Phys. Rev. B **89**, 094419 (2014).

[23]J. F. Ziegler, M. D. Ziegler, and J. P. Biersack, Nucl. Instrum. Methods Phys. Res., Sect. B **268**, 1818 (2010).

[24]S. J. Hak, Ph.D. thesis, University of Groningen, The Netherlands, 2006 (see http://www.rug.nl/research/portal/files/2849285/09_thesis.pdf).

[25]S. Vives and C. Meunier, Thin Solid Films **518**, 3748 (2010).

[26]S. Kim, H. Y. Jeong, S.-Y. Choi, and Y.-K. Choi, Appl. Phys. Lett. **97**, 033508 (2010).

[27]P. K. Sarkar, M. Prajapat, A. Barman, S. Bhattacharjee, and A. Roy, J. Mater. Sci. **51**, 4411 (2016).

[28]Y. M. Lu, M. Noman, Y. N. Picard, J. A. Bain, P. A. Salvador, and M. Skowronski, J. Appl. Phys. **113**, 163703 (2013).

[29]M. K. Yang, H. Ju, G. H. Kim, J.-K. Lee, and H.-C. Ryu, Sci. Rep. **5**, 14053 (2015).

[30]P.-K. Yang, C.-H. Ho, D.-H. Lien, J. R. D. Retamal, C.-F. Kang, K.-M. Chen, T.-H. Huang, Y.-C. Yu, C.-I. Wu, and J.-H. He, Sci. Rep. **5**, 15087 (2015).